Research Article Vol. 34, No. 10 / 18 May 2026 / Optics Express 17634
Optics EXPRESS

Image feature-based aircraft wake identification with coherent Doppler wind lidar

HAO WU,[1,2] HAOYU YANG,[1,2] JINLONG YUAN,[1,2,3,*] XU ZHOU,[3] YUANHAO GU,[1,2] JIAXIU LIU,[1,2] JIAWEI QIU,[1,2] JIADONG HU,[1,2] HAIYUN XIA,[1,2,4] AND ZHIYUAN JIN[5]

[1]*State Key Laboratory of Climate System Prediction and Risk Management, Nanjing University of Information Science and Technology, Nanjing 210044, China*
[2]*School of Atmospheric Physics, Nanjing University of Information Science and Technology, Nanjing 210044, China*
[3]*CMA Weather Modification Center, Beijing 100081, China*
[4]*Institute of Lidar Technology, GuangZai Co., Ltd., Hangzhou 310005, China*
[5]*CAAC Central and Southern Regional Administration, Guangzhou 510405, China*
[*]*yuanjinlong@nuist.edu.cn*

Abstract: Aircraft wake vortices present substantial risks to aviation safety and significantly constrain airport operational efficiency. To address this, we propose a lightweight wake vortex identification method that exploits the hue, saturation, and value (HSV) color space combined with image texture features. This method relies neither on pre-collected datasets nor on preset parameters, and enables accurate and rapid localization of the wake vortex core region. By transforming lidar wind field data into the HSV color space, the algorithm leverages the high sensitivity of hue and saturation to velocity gradients, thereby enhancing the extraction of vortex core contours. Validation against numerical simulations yields root mean square errors (RMSE) of 2.57 m and 6.08 m for the left and right vortex core positions, respectively, with a circulation retrieval RMSE of 38.14 m^2/s (10.37%). Field experiments conducted at Guangzhou Baiyun International Airport confirm the method's capability to accurately capture the evolution of high-altitude wakes and complex low-altitude ground effects. Crucially, the proposed approach significantly reduces computational complexity while maintaining high identification accuracy, offering a viable solution for real-time airport wake vortex monitoring systems.

1. Introduction

Wake vortex, an aerodynamic phenomenon generated by aircraft wings during lift production, poses a significant threat to the flight safety of following aircraft through its induced turbulent flow field. The static wake vortex separation standards implemented by the International Civil Aviation Organization (ICAO) have been relatively conservative, as they do not adequately account for meteorological factors such as atmospheric turbulence that accelerate wake vortex decay. This conservatism has consequently constrained the operational efficiency of busy airports [1]. To mitigate these limitations, Aircraft Wake Turbulence Reclassification (RECAT) programs have been implemented in Europe, the United States [2], and China [3]. Consequently, dynamic wake separation (DWS), which relies on precise prediction of vortex behavior, has emerged as a critical technology for enhancing capacity. This shift has created an urgent demand for high-precision, real-time wake vortex detection systems.

Early detection efforts utilized C-band and X-band radars to identify vortices via backscattering intensity and Doppler spectral characteristics [4,5]. However, microwave radars rely heavily on precipitation particles, rendering them ineffective in clear-air conditions. In contrast, Doppler wind lidar offers high spatiotemporal resolution and clear-air detection capabilities, making it one of the two wake vortex measurement methods recognized by ICAO [6]. Extensive field

#590118 https://doi.org/10.1364/OE.590118
Journal © 2026 Received 14 Jan 2026; revised 8 Apr 2026; accepted 22 Apr 2026; published 5 May 2026

Optics EXPRESS

campaigns by NASA [7], DLR [8], and ONERA [9] have validated lidar's efficacy and provided empirical data for establishing dynamic separation standards. Similarly, research institutions in China have conducted significant validation studies using high-resolution lidar at major airports [6,10,11].

With the advancement of lidar detection technology, wake vortex parameter retrieval has become a focal research area. Holzäpfel et al. proposed a classic method for estimating the circulation of wake vortices [12]; Köpp et al. developed the velocity envelope method (VE) using a 2μm Doppler lidar to achieve vortex center localization [13]; Smalikho et al. proposed the radial velocity method (RV), which shows good adaptability under weak turbulence conditions [14]. Subsequently, Li et al. proposed a path integral method (PI), which has demonstrated higher accuracy in vortex core localization and circulation estimation [15]. While these approaches have achieved significant success, the high computational cost associated with these iterative algorithms make it challenging to meet the strict real-time efficiency required by airport operations.

Recent advancements in artificial intelligence (AI) have offered promising solutions to these challenges. Wu et al. proposed a V2D wake vortex visualization system enabling real-time parameter display [6]; Pan et al. improved VGG16 network for wake vortex classification, which outperforms traditional machine learning algorithms such as support vector machines (SVM) [16]; and Wei et al. introduced a dynamic Bayesian network model that further enhances retrieval accuracy [17]; Stephan et al. proposed a two-stage detection pipeline integrating YOLOv4 with a regressive convolutional neural network, and combined a novel projection method to estimate the circulation and vortex core radius, thus achieving single-target tracking as well as high-precision and rapid characterization of aircraft wake vortices [18]; Wartha et al. established a training framework for lidar simulated data based on large eddy simulation, which further improves the retrieval accuracy and cross-scenario generalization capability of the wake vortex processing model [19,20].These deep learning methods have significantly enhanced the robustness of aircraft wake detection and demonstrated superior recognition accuracy compared to traditional methods in a variety of typical scenarios. However, the early stage of its training process requires high quality datasets and incurs substantial costs.

To address these challenges, this work proposes a lightweight detection method for aircraft wake based on HSV color space transformation and image texture features. By converting radial wind field data into image signals, we leverage the distinct spectral separability of the HSV space to enhance the contrast between vortex signatures and background noise. This approach enables rapid, accurate vortex core localization without complex fluid dynamics inversion or heavy neural network architectures. We validate the method using both simulated datasets and field measurements from Guangzhou Baiyun International Airport.

The remainder of this paper is organized as follows: Section 2 details the principles of the wake vortex detection algorithm based on HSV color space and image features; Section 3 validates the algorithm performance using simulated datasets and applies it to field wake vortex detection experiments at operational airports.

2. Method and data

The proposed method identifies aircraft wake by extracting image features from the core regions. The procedure consists of four main steps, as illustrated in Fig. 1. Step 1: Two-dimensional wind velocity fields are constructed through numerical simulation, and a virtual lidar dataset is generated using the time-domain analysis method [21]. Step 2: The radial velocity maps are processed using HSV color space transformation to extract image representations of the vortex core regions. Step 3: Wake vortices are identified and its characteristic parameters are computed. Step 4: Algorithm parameters are optimized based on the identification results, and error analysis is performed.

Optics EXPRESS

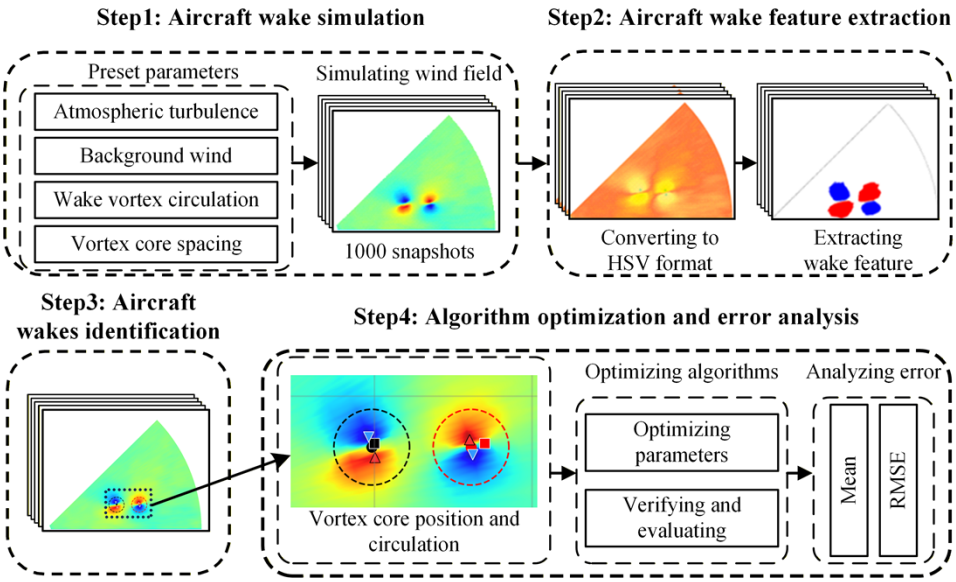

Fig. 1. Algorithm flowchart of a lightweight aircraft wake vortex detection method. The method consists of four main steps: (1) aircraft wake simulation, (2) aircraft wake feature extraction, (3) aircraft wake identification and parameter computation, and (4) algorithm optimization and error analysis.

2.1. *Wake vortex dataset construction with simulation*

To validate the effectiveness of the proposed method and optimize parameters, a wake vortex velocity field dataset is first constructed. The velocity field is obtained through linear superposition of three components: the initial wake vortex field ($\overrightarrow{U_w}$), the atmospheric turbulence field ($\overrightarrow{U_t}$), and a uniform background wind field ($\overrightarrow{U_b}$), expressed as:

$$\overrightarrow{U} = \overrightarrow{U_w} + \overrightarrow{U_t} + \overrightarrow{U_b} \tag{1}$$

where $\overrightarrow{U_w}$ is determined by the wake vortex parameterized model;$\overrightarrow{U_t}$ is a random velocity field generated based on the Von Kármán spectrum model [22]; and $\overrightarrow{U_b}$ is set along the aircraft spanwise direction (y-axis) with wind speeds uniformly sampled from the interval [−3, 3] m/s, where negative values indicate wind direction opposite to the y-axis and positive values indicate the same direction.$\overrightarrow{U_w}$ is described using the Hallock-Burnham vortex pair model [23], which is the linear superposition of the left vortex $\overrightarrow{U_L}$ and the right vortex $\overrightarrow{U_R}$:

$$\overrightarrow{U_w} = \overrightarrow{U_L} + \overrightarrow{U_R} \tag{2}$$

The tangential velocity magnitude for each individual vortex is given by [24]:

$$V_\theta = \frac{\Gamma_0}{2\pi} \cdot \frac{r}{r^2 + r_c^2} \tag{3}$$

where r represents the distance from a point on the vortex cross-section to the vortex core position, $r_c = 0.052 b_0$ is the vortex core radius, and b_0 is the vortex core spacing.

Vortex circulation is a critical physical quantity characterizing the strength of the wake vortex generated behind an aircraft, representing the rotational intensity of the vortex. The initial

Optics EXPRESS

circulation Γ_0 is primarily determined by the aircraft weight Mg, wingspan B, and flight speed V [24], and its expression is as follows:

$$\Gamma_0 = \frac{Mg}{\rho s B V} \tag{4}$$

where ρ represents the air density around the aircraft, and s denotes the load factor under the elliptical wing assumption, with a value of approximately $\pi/4$.

Simulated lidar detection results are obtained using the time-domain analysis method [21,25]. The principle of the time-domain analysis method is that the aerosol scatterers within the detection range are divided into several slices of equal thickness along the beam propagation axis. Aerosol particles in each slice have the identical motion velocity and direction, with a constant scattering coefficient. The echo signals of each layer are stacked and spliced in chronological order to establish a time-domain model of the echo signals within the effective detection range:

$$\begin{aligned} i(t) = {} & 2\Re \exp(j2\pi\nu_M t_j)\times \\ & \sum_N a_j[\eta_s P_{LO} P_T(t_j - 2r_j/c)T^2(r_j)\beta(r_j)\Delta r(A_r/r_j^2)]^{1/2} \exp(-j2k v_j^r t_j) \end{aligned} \tag{5}$$

where $i(t)$ denotes the heterodyne current within the range gate at time t, ν_M is the frequency shift of the acousto-optic modulator (AOM), t_j is the sampling time of the atmospheric wind field node j, P_{LO} is the local oscillator optical power, η_s is the total optical efficiency of the system, c is the speed of light, A_r is the telescope receiving area, k is the wavenumber of the laser emitted by the virtual wind lidar, and a_j is the random factor corresponding to the speckle effect of the echo signal. N represents the total number of nodes between two atmospheric wind field nodes within the detection range, and Δr is the slice thickness. $T^2(r_j)$ and $\beta(r_j)$ denote the transmissivity and backscattering coefficient at the radial position r_j, respectively.v_j^r represents the initial wind speed at the radial position r_j. The parameters of the virtual lidar are summarized in Table 1.

Table 1. The virtual lidar parameters

Parameter	Value
Laser wavelength	1550 nm
Pulse duration	100 ns
Transmitted pulse energy	100 μJ
Sampling frequency	250 MHz
Telescope diameter	80 mm
Local oscillator light power	0.1 mW
Backscattering coefficient	$8 \times 10^{-6}\,\mathrm{m^{-1}sr^{-1}}$
Atmospheric transmittance	0.8

Figure 2 is a schematic diagram of the principle of lidar range-height display (RHI) scanning to detect the wake turbulence of an aircraft during take-off. The lidar is positioned at point O, and radial velocity measurements of the aircraft wake are acquired by scanning the XOY plane. The parameters of the simulated dataset for wake vortex velocity field are summarized in Table 2.

2.2. HSV-based wake vortex detection algorithm

This study proposes a wake vortex feature extraction method based on image characteristics. First, the raw radial velocity observations from lidar in polar coordinates are mapped onto a uniform grid in Cartesian coordinates through linear interpolation, forming a structured wind field matrix $V_{grid}(x, y)$.To optimize the dynamic range of the velocity field and enhance the distinguishability

Optics EXPRESS

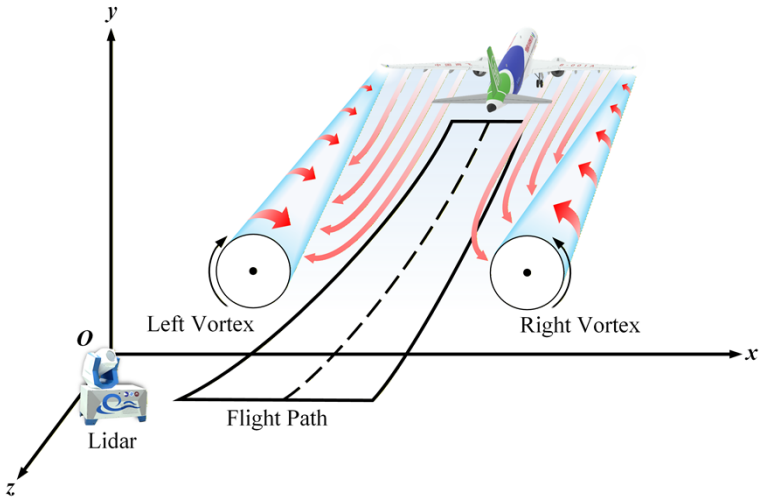

Fig. 2. Schematic of wake vortex velocity model and RHI scanning configuration.

Table 2. The simulated dataset parameters

Parameter	Value
Turbulence energy dissipation rate	0.02 m^2/s^3
Background wind velocity	-3~3 m/s
Wing span	35~80 m
Vortex spacing	27~63 m
Vortex circulation	239~700 m^2/s

of weak and strong velocities, a symmetric piecewise exponential mapping is first applied to $V_{grid}(x, y)$, and then a color mapping function $M_{color} : R \rightarrow R^3$ is introduced to transform the scalar radial velocity field into a pixel matrix I_{RGB} in RGB color space:

$$I_{RGB}(x, y) = M_{color} \cdot [V_{grid}(x, y);\ C_{bar}] \tag{6}$$

where $C_{bar} = \{V_T, \gamma\}$ denotes the parameter set of the symmetric piecewise exponential mapping and colormap. V_T denotes the transform velocity threshold and γ is the exponential adjustment coefficient. During the mapping process, the radial velocity is first subjected to a piecewise exponential nonlinear transformation, with the transformation relationship given by:

$$V_{trans} = \mathrm{sgn}(V_{grid}) \cdot \begin{cases} V_T \left(\frac{|V_{grid}|}{V_T} \right)^{\gamma}, & |V_{grid}| < V_T \\ V_T \left(\frac{|V_{grid}|}{V_T} \right)^{1/\gamma}, & |V_{grid}| \geq V_T \end{cases} \tag{7}$$

where sgn( ) denotes the sign function, which is adopted to retain the velocity direction information. Subsequently, the transformed velocity V_{trans} is mapped to the RGB color space.

Exponential mapping stretches the amplitude of high-velocity regions to avoid color oversaturation, and meanwhile compresses that of low-velocity regions to attenuate the background wind field and atmospheric turbulence, thereby highlighting subtle wake flow details. This enables more effective extraction of image features. The selected colormap not only distinguishes wind speed magnitudes but also provides maximum spectral separability between positive and negative velocity regions through its hue distribution, with red corresponding to positive velocities and

Optics EXPRESS

blue to negative velocities. This step transforms the physical velocity gradient into an image-based color gradient.

Since luminance and chrominance information are highly coupled in RGB color space, threshold-based segmentation directly applied to RGB images is susceptible to background noise interference [26]. Therefore, this study further transforms the RGB representation into HSV color space. Let *(R, G, B)* denote the normalized pixel components:

$$\begin{aligned} &R' = \tfrac{R}{255}; \quad G' = \tfrac{G}{255}; \quad B' = \tfrac{B}{255}, \\ &C_{\max} = \mathrm{MAX}(R', G', B'), \\ &C_{\min} = \mathrm{MIN}(R', G', B'), \\ &\Delta = C_{\max} - C_{\min}, \end{aligned} \tag{8}$$

The transformation model for hue (H), saturation (S), and value (V) in HSV color space is given as follows [27]:

$$\begin{aligned} H &= \begin{cases} 60^\circ \cdot \left(\frac{G'-B'}{\Delta} + 0\right), & C_{\max} = R' \\ 60^\circ \cdot \left(\frac{B'-R'}{\Delta} + 2\right), & C_{\max} = G' \\ 60^\circ \cdot \left(\frac{R'-G'}{\Delta} + 4\right), & C_{\max} = B' \end{cases}, \\ S &= \begin{cases} 0, & C_{\max} = 0 \\ \frac{\Delta}{C_{\max}}, & C_{\max} \neq 0 \end{cases}, \\ V &= C_{\max}, \end{aligned} \tag{9}$$

Regarding threshold selection, this study establishes physical criteria based on wake vortex fluid dynamics characteristics. Research by Robins et al. indicates that for medium-sized aircraft with a wingspan of approximately 30 m (such as the DC-9), a wake circulation of 75 m^2/s poses a potential flight safety hazard, while 150 m^2/s represents a critical hazardous threshold [28]. To balance background interference against the risk of missing small aircraft wake vortices, this method adopts a critical circulation threshold of 150 m^2/s, consistent with the DC-9-sized wingspan of the Airbus A320 (35.8 m). The characteristic integration radius of 15 m is selected, as recommended by [29], and the corresponding critical radial velocity derived from $\Gamma(r) = 2\pi v_t(r)$ [12] is approximately 1.6 m/s. Therefore, the velocity threshold V_T of 1.6 m/s is established to compress lower wind speeds, thereby making weak wake regions easier to distinguish from the background wind field. By applying an exponential transformation, wind speeds below this threshold can be more readily segmented using the HSV color model. Concurrently, the initial image recognition velocity threshold V_m was also set to 1.6 m/s. Finally, the HSV value corresponding to V_m is calculated as the segmentation threshold.

When $V_T = 1.6\ m/s$, the relationship between the value of γ and the recognition rate of vortex is shown in Fig. 3. The recognition rate reaches its maximum at $\gamma = 1.65$. Therefore, $\gamma = 1.65$ is selected for identification.

Feature extraction is performed on the HSV-formatted images using thresholds corresponding to positive and negative radial velocities [30], generating contour images of the positive and negative velocity regions. Figure 4 shows the extracted core region contours of the wake vortex through image feature processing, where red regions correspond to positive velocity cores and blue regions correspond to negative velocity cores. This provides the foundation for subsequent parameter retrieval.

Optics EXPRESS

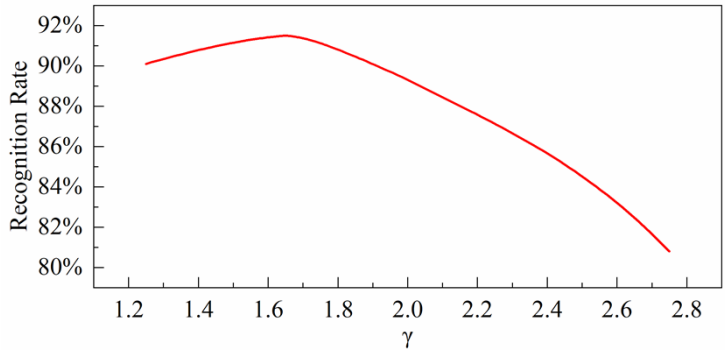

Fig. 3. Relationship between different values of γ and recognition rate.

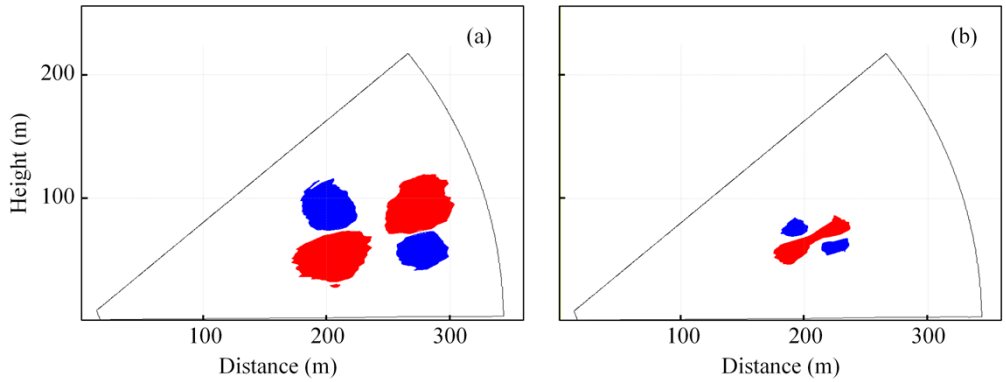

Fig. 4. Wake vortex core region identification results. (a) Large vortex separation case, (b) Small vortex separation case.

2.3. *Wake vortex core localization and parameter retrieval*

To accurately pinpoint the vortex core centers from the HSV-segmented contours, it is essential to filter out background noise. First, connected component analysis is performed on the binary images of positive and negative velocities extracted in the previous section. The area of each connected component is calculated, and the two largest regions are retained as candidate positive and negative velocity cores. Aircraft wake flows exhibit distinct geometric features in the images. After the core regions of positive and negative velocities are acquired, the presence of an aircraft wake flow can be determined based on these geometric features. To determine the region centers, the minimum bounding rectangle method is employed to obtain the geometric center of each connected component.

To analyze the spatial distribution characteristics of the positive and negative velocity regions, this paper sorts and pairs the positive and negative velocity regions according to the x-axis coordinates of the region centers. The positive-negative velocity region pair with a smaller coordinate is denoted as Pair 1 (V_1^+, V_1^-), and the pair with a larger coordinate is denoted as Pair 2 (V_2^+, V_2^-).Let the center coordinate of each region be (x_c, y_c), and the span of its minimum bounding rectangle on the x-axis be denoted as interval X. The following spatial relationship judgments are performed on the two pairs:

First, for any Pair $i(i = 1, 2)$, check whether there is an overlapping portion between the positive and negative velocity regions within the pair in the horizontal direction. This is verified by

Optics EXPRESS

checking for an intersection between the x-axis spans of their minimum bounding rectangles ($X(V_i^+) \cap X(V_i^-) \neq \emptyset$).

Second, check the relative positional relationship of the two pairs in the y-axis direction, respectively. Determine whether Pair 1 satisfies $y_c(V_1^-) > y_c(V_1^+)$, and whether Pair 2 satisfies $y_c(V_2^+) > y_c(V_2^-)$.

If all the above conditions are satisfied simultaneously, it is determined that an aircraft wake exists at the current time.

After identifying valid wake vortex regions, a velocity extremum-based localization method is employed. Specifically, the vortex core position is determined as the geometric midpoint between the maximum velocity point in the positive velocity region and the minimum velocity point in the negative velocity region. The vortex core position is calculated as:

$$x_{Rck} = \frac{x_{Maxk} + x_{Mink}}{2}, \quad y_{Rck} = \frac{y_{Maxk} + y_{Mink}}{2} \tag{10}$$

where (x_{Rck}, y_{Rck}) represents the coordinates of the *k-th* vortex core position; (x_{Maxk}, y_{Maxk}) represents the coordinates corresponding to the maximum radial velocity in the *k-th* positive velocity region, and (x_{Mink}, y_{Mink}) represents the coordinates corresponding to the minimum radial velocity in the *k-th* negative velocity region.

The dataset constructed by us contains aircraft of various types, such that fixed aircraft parameters cannot be adopted for iterative calculation in circulation estimation. In addition, key information including aircraft models cannot be obtained in real time from actual airport scan results. Thus, the method proposed by Gao et al. is selected for circulation estimation [29]. We select multiple measurement units within the range of 15 m ~ $b_0/2$ to construct a system of linear equations, and solve for the circulations Γ_1 and Γ_2 using the linear least squares method.

The data is transformed into the Cartesian coordinate system. First, calculate the intersection points between the circle centered at the left vortex core with a radius of 15 m and the sector centered at the lidar with a radius equal to the distance from the lidar to the left vortex core. These points serve as the initial upper and lower measurement units $V_1^r(x_1, y_1)$ and $V_{-1}^r(x_{-1}, y_{-1})$.

Since the distance from the lidar to the target is much larger than the elevation angle difference between the measurement units, the radial components of the background wind can be regarded as identical. Subtracting $V_{-1}^r(x_{-1}, y_{-1})$ from $V_1^r(x_1, y_1)$ eliminates the background wind term, yielding the velocity difference ΔV_1:

$$\Delta V_1 = V_1^r - V_{-1}^r \tag{11}$$

ΔV_1 is affected by the circulation Γ_1 of the left vortex and the circulation Γ_2 of the right vortex, and can be expressed as:

$$\Delta V_1 \approx \Psi_1 \cdot \Gamma_1 + \Psi_2 \cdot \Gamma_2 \tag{12}$$

where Ψ_1 and Ψ_2 represent the influence coefficients of the left and right vortices on the measurement points, which can be derived from the Hallock–Burnham relation as:

$$\Psi_1 = \frac{1}{2\pi}\left[\frac{y_1 x_{Rc1} - x_1 y_{Rc1}}{d_{11}^2 + r_c^2} \cdot \frac{1}{R_1} - \frac{y_{-1} x_{Rc1} - x_{-1} y_{Rc1}}{d_{21}^2 + r_c^2} \cdot \frac{1}{R_{-1}}\right] \tag{13}$$

$$\Psi_2 = -\frac{1}{2\pi}\left[\frac{y_1 x_{Rc2} - x_1 y_{Rc2}}{d_{12}^2 + r_c^2} \cdot \frac{1}{R_1} - \frac{y_{-1} x_{Rc2} - x_{-1} y_{Rc2}}{d_{22}^2 + r_c^2} \cdot \frac{1}{R_{-1}}\right] \tag{14}$$

In the equation, (x_{Rc1}, y_{Rc1}) and (x_{Rc2}, y_{Rc2}) denote the coordinates of the left and right vortex cores respectively, r_c is the vortex core radius, d_{11} and d_{12} represent the distances from $V_1^r(x_1, y_1)$ to the left and right vortex cores respectively, d_{21} and d_{22} represent the distances

Optics EXPRESS

from $V_{-1}^{r}(x_{-1}, y_{-1})$ to the left and right vortex cores respectively, R_1 and R_{-1} represent the distances from measurement units to the lidar. In the absence of aircraft type information, the proposed method calculates r_c using the vortex core spacing and substitutes it into the circulation calculation formula.

Select L groups of measurement units to construct multiple sets of linear equations:

$$\begin{bmatrix} \Delta V_1 \\ \Delta V_2 \\ \vdots \\ \Delta V_L \end{bmatrix} = \begin{bmatrix} \Psi_1^1 & \Psi_1^2 \\ \Psi_2^1 & \Psi_2^2 \\ \vdots & \vdots \\ \Psi_L^1 & \Psi_L^2 \end{bmatrix} \begin{bmatrix} \Gamma_1 \\ \Gamma_2 \end{bmatrix} \tag{15}$$

Γ_1 and Γ_2 can be solved using the linear least squares method.

In practical scenarios, particularly during early evolution or at long detection ranges, the vortex core spacing may fall below the lidar's spatial resolution. This results in a blending of opposing velocity signatures, rendering conventional threshold segmentation ineffective, as shown in Fig. 4(b). To address this, we proposed an adaptive threshold optimization strategy. Upon detecting the fusion of velocity regions indicated by an anomalous drop in connected components or a surge in area, the algorithm adaptively raises the wind speed threshold. This process progressively contracts the segmentation boundaries to strip away low-velocity peripheries, thereby successfully isolating the distinct left and right vortex cores.

Two representative sets of simulation data are selected for testing. $V_T = 1.6\ m/s$, $\gamma = 1.65$, and $V_m = 1.6\ m/s$ are adopted in the experiment. The identification results are presented in Fig. 5. Figure 5(a) displays the scenario with wide vortex core spacing. Following HSV color space conversion and feature extraction (corresponding to Fig. 4(a)), the algorithm clearly isolates the left and right vortex cores from the background, yielding well-defined contours. Conversely, in the case of narrow core spacing shown in Fig. 5(b), the positive velocity regions appear merged due to the limited scanning resolution of the lidar (refer to Fig. 4(b)). By raising the velocity threshold, the algorithm separates the independent cores. The optimization process is described in detail below.

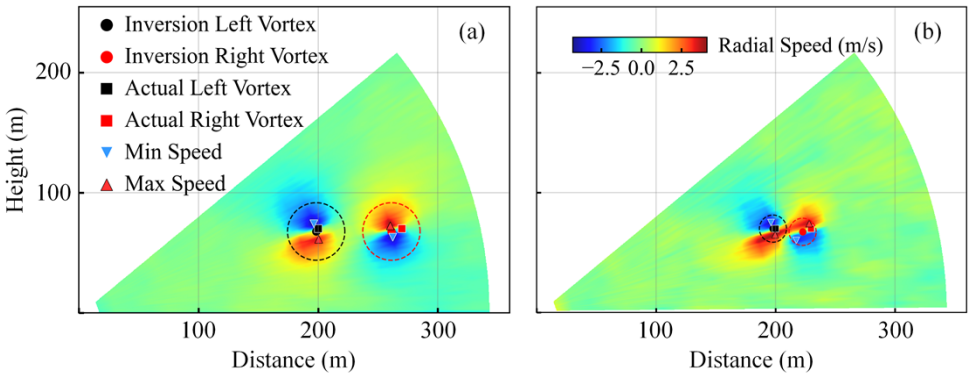

Fig. 5. Identification results of typical vortex core positions. (a) Results for large core spacing. (b) Results for narrow core spacing.

Figure 6(a) presents the result obtained by processing the case in Fig. 5(b) using the initial image recognition velocity threshold $V_m = 1.6m/s$. At this point, the algorithm detects vortex core merging and gradually increases the image recognition velocity threshold. A step size of 0.3 m/s is adopted in this optimization process, and the contraction process is illustrated in

Optics EXPRESS

Figs. 6(b)-(e). When $V_m = 3.1m/s$, the left and right vortex cores are successfully separated, and the wake vortex identification is completed. As demonstrated by the optimized results in Fig. 5(b) and Fig. 6(f), the method successfully achieves the effective separation and localization of the compact twin-vortex structure. During this process, the algorithm only needs to calculate the HSV threshold corresponding to the increased image recognition velocity threshold, which does not introduce significant additional computational cost. This optimization significantly enhances the algorithm's robustness in identifying compact twin-vortex structures. However, such structures with small vortex core spacing and mutual coalescence can lead to indistinct dual-peak velocity structures along the lidar line of sight, which tends to cause the failure of the RV method.

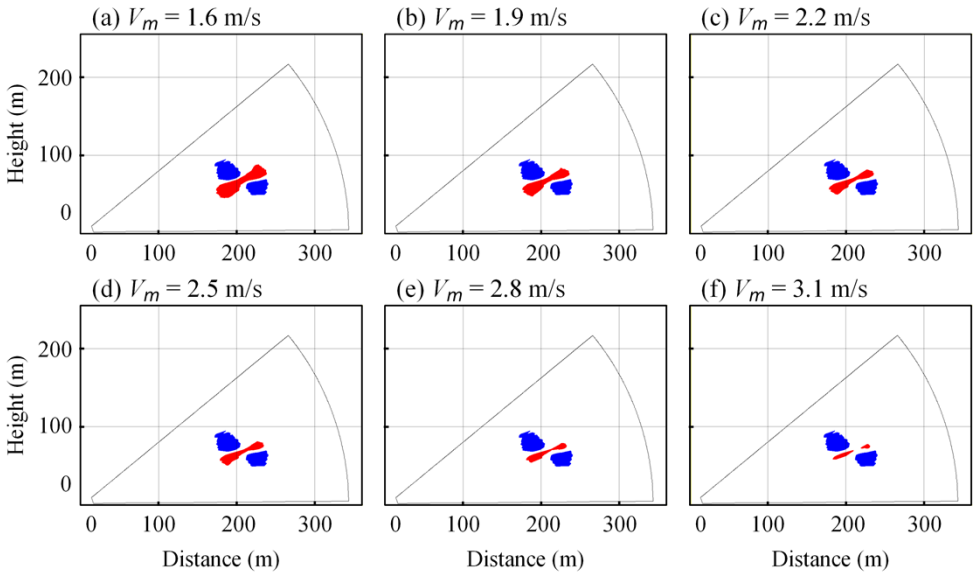

Fig. 6. Adaptive threshold optimization process in situation of vortex core merging, with V_m ranging from 1.6 m/s to 3.1 m/s in panels (a)-(f).

3. Results and discussion

The evaluation is conducted in two distinct phases. First, the simulated datasets are utilized to statistically analyze the algorithm's localization accuracy and parameter retrieval error. Second, lidar observational data are applied to validate the algorithm's applicability under complex conditions, specifically focusing on typical high-altitude evolution and ground effect scenarios.

3.1. Performance evaluation under varying conditions

To quantitatively evaluate the algorithm's retrieval performance under varying vortex core spacings and background flow fields, a total of 1,000 simulated datasets were utilized for testing, as shown in the dataset [31]. Finally, the average single-frame running time of the algorithm on a personal laptop is 0.7 seconds. The laptop is equipped with an Intel i5-12500H CPU and 16.0 GB of memory, and runs under the Python 3.12 environment. Under the same configuration and environment, the average running time of the RV method is 5.7 seconds. As illustrated in Fig. 7(a), statistical results indicate that the mean error for the left vortex core position is 2.50 m (corresponding RMSE = 2.57 m), while that for the right core is 5.59 m (corresponding RMSE = 6.08 m). The localization error for the right vortex is slightly higher than for the left; this is

Optics EXPRESS

primarily attributed to the placement of the virtual lidar on the left side of the wake, which results in a higher sampling density for the left vortex. Overall, the localization errors are confined within the magnitude of the lidar's range resolution.

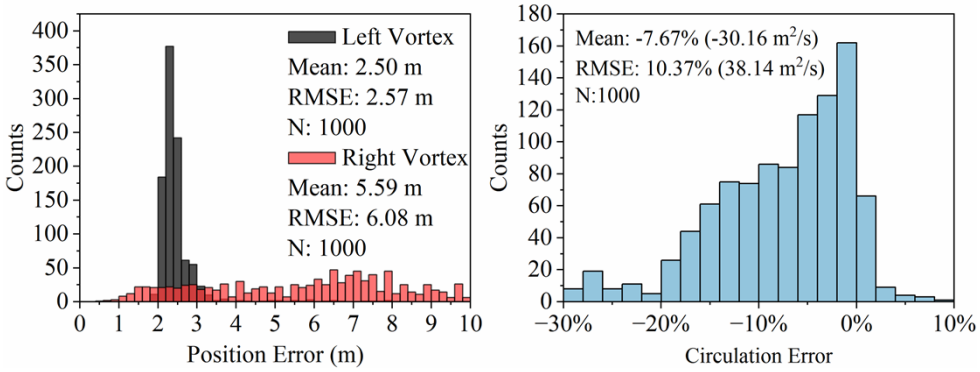

Fig. 7. Statistical evaluation results. (a) Error analysis of vortex core localization. (b) Error analysis of circulation retrieval.

Regarding circulation, as depicted in Fig. 7(b), the deviations cluster around -30.16 m^2/s. Notably, the retrieved circulation tends to be underestimated due to the range resolution effect. With a mean circulation error of -7.67% and an RMSE of 10.37%, the results demonstrate that the proposed method maintains high retrieval credibility without requiring complex fluid dynamics iterations. The recognition statistics of the proposed method and the RV method are summarized in Table 3.

Table 3. Recognition statistics of the proposed method and the RV method

Parameter	Proposed method	RV method
Left Vortex Mean	2.50 m	2.16 m
Left Vortex RMSE	2.57 m	2.15 m
Right Vortex Mean	5.59 m	5.33 m
Right Vortex RMSE	6.08 m	6.24 m
Circulation Mean	-7.76% (-30.16 m^2/s)	-4.40% (-17.72 m^2/s)
Circulation RMSE	10.37% (38.14 m^2/s)	16.58% (75.12 m^2/s)

The vortex core positioning error of the proposed method is very close to that of the RV method. In terms of circulation estimation, the circulation RMSE of the proposed method is 10.37% (38.14 m^2/s), while that of the RV method using the same dataset is 16.58% (75.12 m^2/s). The RV method calculates circulation through iteration with preset parameters, and the results fluctuate around the actual circulation values. Therefore, the RV method yields a lower circulation mean but a larger circulation RMSE. This validates the feasibility of the proposed method. Next, the proposed method is applied to field tests to verify its feasibility in practical scenarios.

3.2. Field experiment application

Field observation experiments were conducted at Guangzhou Baiyun International Airport (23.3925°N, 113.2989°E) in November 2022. As one of China's major gateway hubs and a core aviation center in the Guangdong-Hong Kong-Macau Greater Bay Area, this airport ranks among the top-tier in the country in terms of passenger throughput. Consequently, aircraft takeoff and landing efficiency acts as a critical factor constraining its operational capacity.

Optics EXPRESS

In this study, a 1550 nm coherent Doppler wind lidar is deployed on the northern side of the west runway, situated 180 m from the runway centerline, as indicated by the red triangle in Fig. 8(a). This lidar is designed for long-range detection, with detailed parameters and applications described in Refs. [32,33]. The key parameters of the lidar are summarized in Table 4.

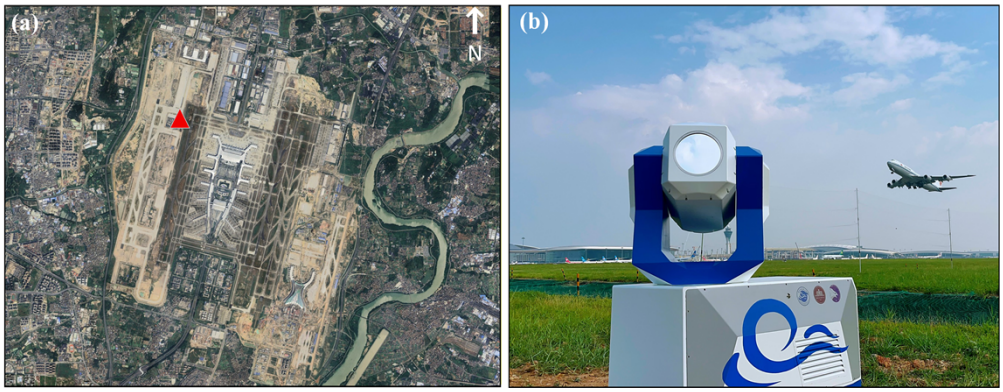

Fig. 8. Experimental site. (a) Map of Guangzhou Baiyun International Airport. (b) The coherent Doppler wind lidar system. The red triangle indicates the lidar deployment location.

Table 4. The 1550 nm coherent Doppler wind lidar parameters

Parameter	Value
Wavelength	1550 nm
Pulse duration	100-800 ns
Transmitter power	1.5 W
Pulse repetition rate	5-10 kHz
Time resolution	1 min/PPI
Range resolution	15~150 m
Telescope diameter	200 mm
Beam full divergence	46 μrad

Specifically, the laser pulse width is switched to 100 ns, yielding a radial range resolution of 15 m, with a temporal resolution of 1 s. The system operates in RHI scanning mode perpendicular to the flight path, as illustrated in Fig. 2. This scanning strategy effectively intercepts wake vortex cross-sections along the flight path, capturing their full lifecycle evolution, including generation, descent, drift, and dissipation. A threshold of -27 dB is first applied to exclude data with a wind speed accuracy lower than 0.2 m/s [34]. Considering the relatively limited influence range of the wake vortex, only data within the range of 0~300 m is analyzed in this study.

Observational data collected on November 12, 2022, from 16:12:29 to 16:13:21 LT, are selected as a representative case for high-altitude wake evolution. As illustrated in Fig. 9, the characteristic signatures of the aircraft wake are first detected within the lidar scanning region at 16:12:29 LT, followed by the continuous evolution of the vortices.

To quantitatively analyze the evolution process, Fig. 10 details the temporal variations in vortex core positions and circulation strengths during this period. L1, L2, and L3 correspond to the left vortex cores at the timestamps shown in Figs. 9(a), 9(b), and 9(c), respectively, with the values in parentheses indicating the circulation strength at each instant. Similarly, R1, R2, and R3

Optics EXPRESS

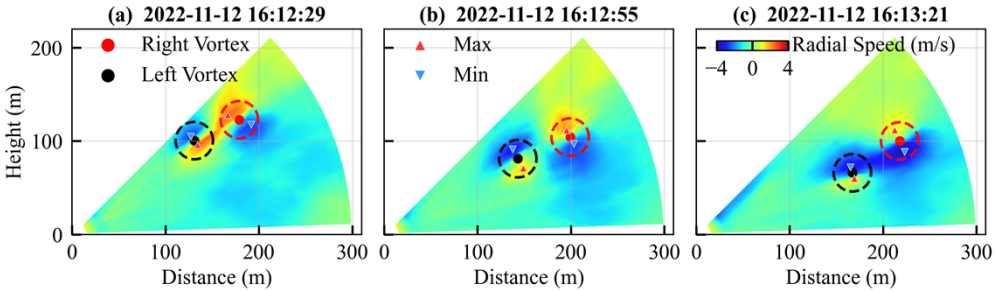

Fig. 9. RHI detection results of a typical high-altitude wake and the corresponding vortex core localization.

represent the right vortex cores. The parenthesized numbers denote their respective circulation strengths.

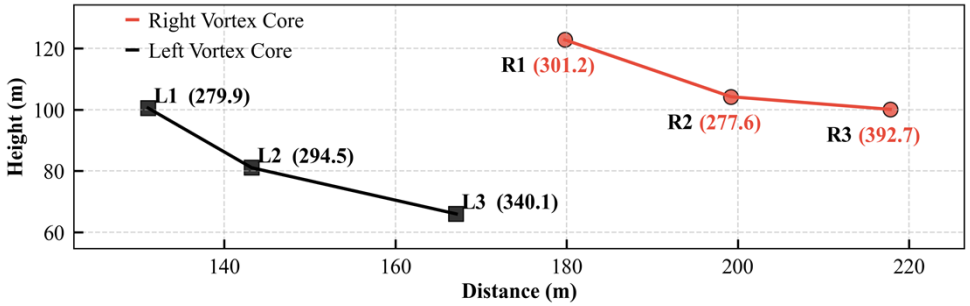

Fig. 10. Evolution of vortex core positions and circulation changes for a typical high-altitude wake. The numbers in parentheses represent the circulation magnitude, with the unit of m^2/s.

During this interval, as illustrated in Figs. 9 and 10, the algorithm effectively localizes and tracks the wake signatures. Both vortex cores exhibit significant descent. Specifically, the left vortex core altitude decreases from 100 m to 66 m (a drop of approximately 34.0%), while the right core decreases from 123 m to 100 m (a drop of 18.7%). In the horizontal direction, both cores drift 37 m away from the lidar. Notably, the presence of a rightward crosswind causes the right vortex core to remain at a higher altitude than the left core.

Simultaneously, the circulation strengths of both vortices display an increasing trend. The left vortex circulation rises from 279.9 m^2/s to 340.1 m^2/s (an increase of 21.5%), and the right vortex circulation increases from 301.2 m^2/s to 392.7m^2/s (an increase of 30.4%). The possible causes of this phenomenon are as follows: The aircraft wake flow may enter the scan plane in a more concentrated manner, resulting in changes to the sampling geometry; the enhanced visibility of the early roll-up phenomenon may lead to an increase in the wake vortex circulation. Under the action of ambient wind, the wake vortices exhibit a state of sinking and outward advection.

To further validate the algorithm's effectiveness under complex dynamic boundary conditions, data collected on the same day from 18:04:25 to 18:05:17 LT were selected as a representative low-altitude case. As illustrated in Fig. 11, the system successfully captured the entire evolution process, from wake generation to the interaction with the ground surface. Figure 12 details the temporal variations in vortex core position and circulation strength during this interval.

During the descent phase (18:04:25–18:04:51 LT), the vortex pair descended rapidly, driven by initial momentum. The left vortex core altitude dropped from 34 m to 13 m, while the right

Optics EXPRESS

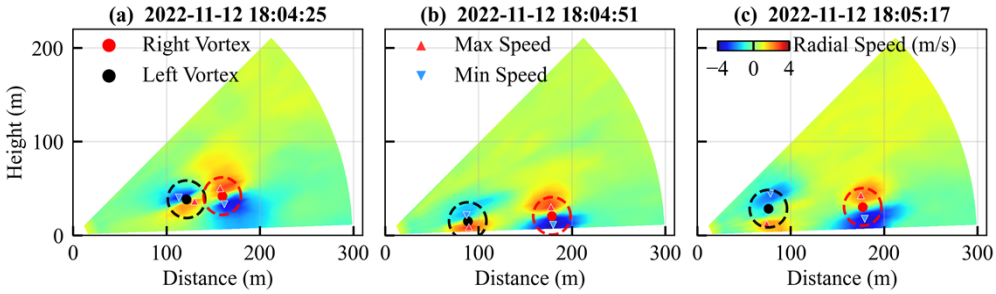

Fig. 11. RHI detection results of a typical low-altitude wake and the corresponding vortex core localization.

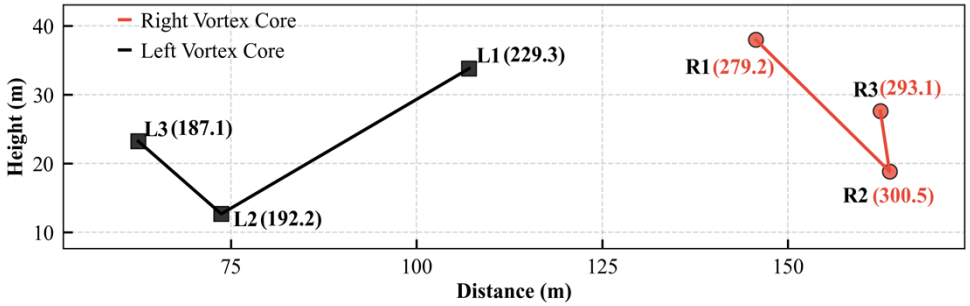

Fig. 12. Evolution of vortex core positions and circulation changes for a typical low-altitude wake. The numbers in parentheses represent the circulation magnitude, with the unit of m^2/s.

core decreased from 38 m to 19 m. In this phase, the left vortex circulation decreased by 16.2%, whereas the right vortex circulation showed a slight increase of 7.6%.

Subsequently (18:04:51–18:05:17 LT), as the wake approached the ground, the descent was impeded and converted into a rebound due to the interaction between the induced velocity field and the ground. The algorithm accurately captured this inflection point: the left core rose to 23 m and the right core to 28 m, representing a rebound amplitude of approximately 47.4%. Regarding circulation evolution, the left vortex exhibited a continuous decreasing trend, indicating an early entry into the dissipation stage. Conversely, the right vortex initially increased before decreasing, signaling a transition from the development phase to the dissipation phase.

In summary, the identified low-altitude aircraft wake vortex demonstrates the complete dynamic process of descent followed by rebound. The continuous decay of the left vortex circulation confirms it is in the dissipation phase, while the trend of the right vortex suggests a transition from development to dissipation.

4. Conclusion

This paper proposes a lightweight localization and parameter retrieval method for aircraft wake vortex. By establishing an HSV mapping mechanism for wind field data of lidar, the method leverages the high sensitivity of Hue and Saturation to vector features to achieve effective identification of wake vortex signals. Validation results indicate that the algorithm achieves high accuracy in vortex core localization and circulation estimation. Field experiments confirmed the algorithm effectiveness in both high-altitude and low-altitude scenarios. Compared with deep learning or traditional numerical methods, the proposed method relies neither on pre-collected

Optics EXPRESS

datasets nor on preset parameters, and enables accurate and rapid localization of the wake vortex core region. This approach avoids the complex fluid dynamics iteration processes required by traditional methods, significantly reducing algorithmic time complexity and providing a real-time monitoring solution for airport operations safety.

While the proposed adaptive threshold optimization strategy partially mitigates the fusion issue of compact twin-vortex structures, challenges remain in resolving fine-scale features due to the spatial resolution limits of the lidar hardware. For weak wind shear, the proposed algorithm can filter out such events via thresholding, thus achieving reliable wake vortex identification. However, strong wind shear may deteriorate the recognition performance and interfere with the accuracy of circulation calculation. In addition, for scenarios with multiple overlapping wakes, the current method cannot accurately count the number of wake vortices. Future work will focus on overcoming physical hardware limitations through super-resolution reconstruction, developing robust identification algorithms for strong wind shear, and further enhancing the detection performance for multiple wake vortices.

Funding. Natural Science Foundation of Jiangsu Province (No.BK20230434); National Natural Science Foundation of China (No.42405137); National Training Program of Innovation and Entrepreneurship for Undergraduates (No.202510300005).

Disclosures. The authors declare no conflicts of interest.

Data availability. Data underlying the results presented in this paper are available in Ref. [31].

References

1. S. Lang, J. Tittsworth, W. Bryant, *et al.*, "Progress on an ICAO wake turbulence re-categorization effort," in *AIAA Atmospheric and Space Environments Conference* (2010), p. 7682.
2. J. N. Hallock and F. Holzäpfel, "A review of recent wake vortex research for increasing airport capacity," Prog. Aeronaut. Sci. **98**, 27–36 (2018).
3. Z. Peng, J. Zhang, T. Xiang, *et al.*, "Benefits derived from arrival management and wake turbulence re-categorization in China," Transp. Res. Rec. **2675**(11), 373–383 (2021).
4. K. Shariff and A. Wray, "Analysis of the radar reflectivity of aircraft vortex wakes," J. Fluid Mech. **463**, 121–161 (2002).
5. Z. Liu, N. Jeannin, F. Vincent, *et al.*, "Modeling the radar signature of raindrops in aircraft wake vortices," Journal of Atmospheric and Oceanic Technology **30**(3), 470–484 (2013).
6. S. Wu, X. Zhai, and B. Liu, "Aircraft wake vortex and turbulence measurement under near-ground effect using coherent Doppler lidar," Opt. Express **27**(2), 1142–1163 (2019).
7. R. Perry, D. Hinton, R. Stuever, *et al.*, "NASA wake vortex research for aircraft spacing," in *35th Aerospace Sciences Meeting and Exhibit* (1997), p. 57.
8. F. Kopp, "Doppler lidar investigation of wake vortex transport between closely spaced parallel runways," AIAA J. **32**(4), 805–810 (1994).
9. D. T. Michel, A. Dolfi-Bouteyre, D. Goular, *et al.*, "Onboard wake vortex localization with a coherent 1.5 microm Doppler LIDAR for aircraft in formation flight configuration," Opt. Express **28**(10), 14374–14385 (2020).
10. C. Shen, W. Tang, H. Gao, *et al.*, "Aircraft wake recognition and strength classification based on deep learning," IEEE J. Sel. Top. Appl. Earth Observations Remote Sensing **16**, 2237–2249 (2023).
11. L. Deng, W. Pan, P. Zhao, *et al.*, "TransCNN: a hybrid framework for aircraft wake vortex detection and safety interval assessment," IEEE Trans. Aerosp. Electron. Syst. **61**(6), 15210–15223 (2025).
12. F. Holzäpfel, T. Gerz, F. Köpp, *et al.*, "Strategies for circulation evaluation of aircraft wake vortices measured by lidar," J. Atmos. Oceanic Technol. **20**(8), 1183–1195 (2003).
13. F. Köpp, S. Rahm, and I. Smalikho, "Characterization of aircraft wake vortices by 2-μm pulsed doppler lidar," J. Atmos. Oceanic Technol. **21**(2), 194–206 (2004).
14. I. N. Smalikho, V. A. Banakh, F. Holzäpfel, *et al.*, "Method of radial velocities for the estimation of aircraft wake vortex parameters from data measured by coherent Doppler lidar," Opt. Express **23**(19), A1194–A1207 (2015).
15. J. Li, C. Shen, H. Gao, *et al.*, "Path integration (PI) method for the parameter-retrieval of aircraft wake vortex by Lidar," Opt. Express **28**(3), 4286–4306 (2020).
16. W. Pan, Y. Leng, H. Yin, *et al.*, "Identification of Aircraft Wake Vortex Based on VGGNet," Wireless Communications and Mobile Computing **2022**, 1–10 (2022).
17. Z. Wei, T. Lu, R. Gu, *et al.*, "DBN-GABP model for estimation of aircraft wake vortex parameters using Lidar data," Chin. J. Aeronaut. **37**(9), 347–368 (2024).
18. A. Stephan, G. Rotshteyn, N. Wartha, *et al.*, "Artificial neural networks for individual tracking and characterization of wake vortices in LIDAR measurements," in *AIAA AVIATION 2023 Forum*, (2023).

Optics EXPRESS

19. N. Wartha, A. Stephan, F. Holzäpfel, *et al.*, "Characterizing aircraft wake vortex position and strength using LiDAR measurements processed with artificial neural networks," Opt. Express **30**(8), 13197 (2022).
20. N. Wartha, A. Stephan, and F. Holzapfel, "Wake vortex lidar measurement processing with large-eddy simulations and machine learning," Opt. Express **33**(12), 26473–26498 (2025).
21. J. Liu, J. Yuan, H. Yang, *et al.*, "Research on impact of range resolutions on wind detection performance using virtual lidar," Opt. Express **33**(15), 32386–32397 (2025).
22. B. Etkin, "Turbulent wind and its effect on flight," J. Aircr. **18**(5), 327–345 (1981).
23. N. N. Ahmad and F. Proctor, "Review of idealized aircraft wake vortex models," in *52nd Aerospace Sciences Meeting*, (2014), pp. 1–28.
24. T. Gerz, F. Holzäpfel, and D. Darracq, "Commercial aircraft wake vortices," Prog. Aeronaut. Sci. **38**(3), 181–208 (2002).
25. P. Salamitou, A. Dabas, and P. H. Flamant, "Simulation in the time domain for heterodyne coherent laser radar," Appl. Opt. **34**(3), 499–506 (1995).
26. P. Ganesan and V. Rajini, "Assessment of satellite image segmentation in RGB and HSV color space using image quality measures," in *2014 International Conference on Advances in Electrical Engineering* (ICAEE, 2014), pp. 1–5.
27. D. Travis, *Effective color displays: Theory and practice* (Academic press London, 1991), Vol. 1991.
28. R. E. Robins and D. P. Delisi, "Potential hazard of aircraft wake vortices in ground effect with crosswind," J. Aircr. **30**(2), 201–206 (1993).
29. H. Gao, J. Li, P. W. Chan, *et al.*, "Parameter retrieval of aircraft wake vortex based on its max–min distribution of Doppler velocities measured by a Lidar," The Journal of Engineering **2019**(20), 6852–6855 (2019).
30. G. Schleyer, G. Lefranc, C. Cubillos, *et al.*, "A new method for colour image segmentation," International Journal of Computers Communications & Control **11**(6), 860–876 (2016).
31. W. Hao, "Aircraft Wake Vortex Dataset," figshare (2026), https://doi.org/10.6084/m9.figshare.31044199.
32. H. Xia, Y. Chen, J. Yuan, *et al.*, "Windshear detection in rain using a 30 km radius coherent doppler wind lidar at mega airport in plateau," Remote Sens. **16**(5), 924 (2024).
33. A. Chen, J. Yuan, H. Yang, *et al.*, "Identification and forecasting of low-level wind shear based on long range Doppler wind lidar," Atmos. Res. **330**, 108558 (2026).
34. C. Wang, H. Xia, M. Shangguan, *et al.*, "1.5 mum polarization coherent lidar incorporating time-division multiplexing," Opt. Express **25**(17), 20663–20674 (2017).